The reference to the final published version of this paper is:

Modeling microstructure evolution in shape memory alloy rods via Legendre wavelets collocation method, He, X., Tong, Z., Du, H., Wang, D., Wang, L., Melnik, R., JOURNAL OF MATERIALS SCIENCE, 54 (23), 14400-14413, 2019

DOI: 10.1007/s10853-019-03927-5

Modeling Microstructure Evolution in Shape Memory Alloy Rods via Legendre Wavelets Collocation Method

Xuan He[1,3], Zheng Tong[2], Haoyuan Du[1], Dan Wang[1], Linxiang Wang[1]*, Roderick Melnik[3,4]

1. State Key Laboratory of Fluid Power and Mechatronic Systems, Zhejiang University, 310027, Hangzhou, China
2. Research Institute of Petroleum Exploration and Development (RIPED), PetroChina, P. O. Box910, No. 20 Xueyuan Road, 100083, Beijing, China
3. MS2Discovery Interdisciplinary Research Institute, Wilfrid Laurier University, Waterloo, ON N2L 3L5, Canada
4. BCAM-Basque Center for Applied Mathematics, Alameda de Mazarredo 14, E-48009 Bilbao, Spain
* Corresponding author: wanglx236@zju.edu.cn

Abstract Microstructures play an important role in the research on shape memory alloys (SMA). By using mathematical modeling tools to study microstructures, it is possible to predict the behaviors of these materials under applied fields. In the current paper, a thermo-mechanical model is proposed to simulate the microstructure of a SMA rod with both fixed and impact boundary conditions via Legendre wavelets collocation method. Because of the good performance of Legendre wavelets basis, this method shows excellent properties in both precision and stability. A detailed numerical algorithm is given and the backward differentiation formula is employed to perform all the simulations in the current paper. Computational simulations are carried out to study the stress induced phase transformation (PT). The dynamics of microstructure evolution, presented at different temperatures, is well captured by our developed technique.

Keywords: Legendre wavelets; shape memory alloy; microstructure; Landau theory; phase transformation.

1 Introduction

Shape memory alloys (SMA) are a kind of well-known smart materials due to their unique thermo-mechanical properties. When the temperature varies, the lattice structure of SMA would switch between austenitic phase (at high temperature) and martensitic phase (at low temperature). The shape memory effect implies that the deformation happened in martensitic phase will be recovered in the austenitic phase when the

SMA is under the appropriate thermal loading. The lattice structure of SMA will also change from austenitic phase to martensitic phase under applied proper mechanical loading at proper temperature, and the lattice will turn back to austenite when the loading is removed. The deformation happened during this process is actual PT which makes the deformation range far beyond the normal elastic deformation, and this phenomenon is known as pseudoelasticity. Due to the unique properties, including the shape memory effect and pseudoelasticity, SMAs are widely applied in medical instruments, aerospace machinery and etc. [1-3].

SMAs have recently been considered for dynamic loading applications such as energy absorbing, vibration damping devices, as well as advanced SMA composite materials [4-6]. Different from that for traditional materials, the simulation of SMA's response under different external loadings is more difficult to accomplish due to the phase transformation, not to mention the existence of complex thermo-elastic coupled effects. Therefore, it is very important to study the microstructure evolution of SMA under different and complex external loadings, which will help us better understand and predict the dynamical response of SMA-based devices in engineering and other applications, and ultimately to control such devices.

The research on SMA models can be mainly divided into two parts: micro-mechanical models and phenomenological ones. The micro-mechanical models are theoretically more convincing from a fundamental theoretical point of view and are attacked by a large number of researchers to investigate various implementation methods [7-9]. Rep-

resentative works about micro-mechanical models were presented by Lagoudas [10-17], and improved by Tanaka [18-20], in which a thermodynamic approach was introduced into phase transformation simulations which made the mechanical model more attractive. However, the computation based on micro-mechanical models is much more demanding than on the phenomenological ones. The computational cost for micro-mechanical models in engineering applications is too expensive. On the other hand, the phenomenological models, such as the models based on the Landau theory, could also lead to very good simulation results, provided we have appropriate constitutive relations. The phenomenological model is often more convenient for researchers to analyze and simulate SMA behavior. The Landau theory was employed to model the SMA microstructure by Falk [21-23]. Afterwards, many researchers made a significant contribution to the phenomenological model of SMA. Sprekels [24] was the first to introduce the thermomechanical laws into the Landau-Ginzburg model. Bubner [25] studied experimentally the thermodynamics response of SMA under deformation-driven conditions. Berti [26] introduced the phase field method to analyze the phase transitions in a non-isothermal situation. Dhote et al [27-32] introduced the isogeometric analysis into phase field model to improve the simulation accuracy. Nowadays, the phenomenological model of SMAs has been improved in many different aspects, and even the 3-D cases could be approximated by using the Landau model [33-35].

In the numerical investigations about SMA structures and devices, the finite element method [11] is the most popular tool due to its ma-

turity and existing commercial software for the purpose, such like COMSOL. However, other numerical methods also have their own advantages in numerical investigations of SMA. Wang [36-39] employed the Chebyshev spectral method to analyze the wave propagation under impact loadings. The simulation made by the spectral method led to new encouraging results in the studies of microstructure evolution. However, computational efficiency is still a huge problem for spectral methods. The combination of wavelet and spectral methods can reduce the computation time effectively [40], therefore it is natural to expect that it should also be promising in modeling microstructure of SMA.

In this work, the Legendre wavelets method (LWM) has been developed and applied to simulate the microstructure evolution of SMAs. Specifically, we focus on the microstructure evolution of a SMA rod under impact loading in a dimensionless form. The wave propagation during the phase transformation for different temperatures are simulated by the Landau theory as well. The wave pattern of SMAs is described well for different internal friction coefficients. The current paper is organized as follows. The thermo-mechanical model of SMA is presented in section 2. A brief introduction to the LWM is given in section 3. Finally, the simulations and analysis of different temperatures are discussed in section 4. The computational and performance analysis are discussed in section 5. Concluding remarks are given in section 6.

2 Mathematical model for SMA

A SMA thin rod with length L is considered as an initial-boundary value problem in the current paper. Functions $u(x,t)$ and $\theta(x,t)$ denote

the displacement and temperature distributions at point x along the rod at time t. The stress $\sigma(x,t)$ is assumed to be dependent only on time and the axial position, so we can treat it as an 1-D problem. With consideration of the internal friction, the momentum and energy balance equations could be formulated in the following form [41]:

$$\begin{aligned} \rho u_{tt} - \sigma_x - \nu u_{xxt} + k_g u_{xxxx} + f = 0, \\ c_v \theta_t = k\theta_{xx} + k_1 \theta \varepsilon \varepsilon_t. \end{aligned} \tag{1}$$

Here ρ is the density of the rod, ν is the viscosity coefficient, k is the heat conductance, c_v is the specific heat capacitance and k_1 and k_g are the material constants, f is the external force. The stress $\sigma(x,t)$ can be related to the strain ε, where $\varepsilon = \frac{\partial u}{\partial x}$, by a nonlinear function $\sigma = \frac{\partial E}{\partial \varepsilon}$, which is used to characterize the properties of the material. The function E is the potential energy function which is constructed on the basis of the Landau theory [25]:

$$\begin{aligned} E = F_0(\theta) + \tfrac{k_1}{2}(\theta - \theta_1)\varepsilon^2 - \tfrac{k_2}{4}\varepsilon^4 + \tfrac{k_3}{6}\varepsilon^6 + \tfrac{k_g}{2}u_{xx}^2, \\ \sigma = k_1(\theta - \theta_1)\varepsilon - k_2\varepsilon^3 + k_3\varepsilon^5, \end{aligned} \tag{2}$$

where k_2, k_3 are the material constants, θ_1 is the reference temperature.

There are two kinds of situations considered in the current investigation. The first is a case with fixed boundary conditions, as follows:

$$\begin{aligned} u(0,t) = 0, \quad & u(L) = 0, \\ u_{xx}(0,t) = 0, \quad & u_{xx}(L,t) = 0, \\ \theta_x(0,t) = 0, \quad & \theta_x(L,t) = 0. \end{aligned}$$

The second one is the impact boundary conditions: the left end of this rod ($x = 0$) is fixed, and its right end($x = L$) is subjected to an impact load. For the sake of clarification of studying the impact induced wave

propagation in the SMA rod, the boundary conditions are formulated as follows [25,37]:

$$\begin{aligned} u(0,t) &= 0, \quad \sigma(L,t) = s(t), \\ u_{xx}(0,t) &= 0, \quad u_{xx}(L,t) = 0, \\ \theta_x(0,t) &= 0, \quad \theta_x(L,t) = 0, \end{aligned}$$

where $s(t)$ is the stress impact loading. The left side of the rod is fixed and the right end is free. The loading is acting on the SMA rod at the right end.

For the numerical investigation, the thermo-mechanical model including martensitic phase transformations for a 1-D microstructure in SMA can be described as follows [25]:

$$\begin{aligned} \rho u_{tt} &= \sigma_x + \nu \frac{\partial}{\partial t}\frac{\partial^2 u}{\partial x^2} - k_g \frac{\partial^4 u}{\partial x^4} + f, \\ \sigma &= k_1(\theta - \theta_1)\varepsilon + k_2\varepsilon^3 + k_3\varepsilon^5, \\ c_v \frac{\partial \theta}{\partial t} &= k\frac{\partial^2 \theta}{\partial x^2} + k_1\theta\varepsilon\frac{\partial \varepsilon}{\partial t}, \end{aligned} \tag{3}$$

with the fixed boundary conditions:

$$\begin{aligned} u(0,t) &= 0, \quad u(L) = 0, \\ u_{xx}(0,t) &= 0, \quad u_{xx}(L,t) = 0, \\ \theta_x(0,t) &= 0, \quad \theta_x(L,t) = 0; \end{aligned}$$

and with the impact boundary conditions:

$$\begin{aligned} u(0,t) &= 0, \quad \sigma(L,t) = s(t), \\ u_{xx}(0,t) &= 0, \quad u_{xx}(L,t) = 0, \\ \theta_x(0,t) &= 0, \quad \theta_x(L,t) = 0. \end{aligned}$$

3 Numerical algorithm based on the Legendre wavelets

The simulation of nonlinear wave propagation based on a system of PDEs is not a trivial task to implement even in 1-D situations, especial-

ly for coupled equations with phase transformation involved. The choice of the algorithm will significantly affect the accuracy of the result. In the current paper, the Legendre wavelets method is employed to perform the numerical analysis.

Wavelets methods can reduce the calculation cost effectively. The Legendre wavelets method is originated from applying the wavelets method to the mother function, which is chosen as Legendre polynomials [42]. The Legendre wavelets family retains the following form:

$$\psi_{n,m}(x) = \begin{cases} \sqrt{m+\frac{1}{2}}\,2^{\frac{k}{2}}P_m(2^k x - 2n + 1), & \text{for } \frac{n-1}{2^{k-1}} \le x \le \frac{n}{2^{k-1}}, \\ 0, & \text{otherwise,} \end{cases} \tag{4}$$

where $m = 0,1,\dots,M-1, n = 1,2,3,\dots,2^{k-1}$, $\sqrt{m+\frac{1}{2}}$ is the coefficient of orthogonality. $P_m(x)$ are Legendre polynomials of order m on interval [-1,1]. It should be noticed that equation (4) gives a set of basis functions for the Legendre spectral method when the parameter $k = 0$. This method could be regarded as dividing the interval [0, 1] into 2^k subintervals, and then applying the Legendre spectral method on each subinterval.

A function $f(x)$ defined on interval [0, 1] can be expanded as Legendre wavelets as follows:

$$f(x) = \sum_{n=1}^{\infty}\sum_{m=0}^{\infty} c_{n,m}\psi_{n,m}(x) = C^T\Psi(x). \tag{5}$$

Here $c_{n,m}$ denotes the inner product of $f(x)$ and $\psi_{n,m}(x)$. If Eq. (5) is truncated, it can be rewritten as

$$f(x) = \sum_{n=1}^{2^{k-1}}\sum_{m=0}^{M-1} c_{n,m}\psi_{n,m}(x) = C^T\Psi(x), \tag{6}$$

where

$$C = [c_{10}, c_{11}, \dots, c_{M-1}, c_{20}, \dots, c_{2M-1}, \dots, c_{2^{k-1}0}, \dots, c_{2^{k-1}M-1}]^T, \quad (7)$$

and

$$\Psi(x) = [\psi_{10}(x), \dots, \psi_{M-1}(x), \psi_{20}(x), \dots, \psi_{2M-1}(x), \dots, \psi_{2^{k-1}0}(x), \dots, \psi_{2^{k-1}M-1}(x)]^T. \quad (8)$$

The vector C in Eq. (7) is called the spectral space coefficient, and C is the only data needed in the calculations that follow.

3.1 Operational matrix of derivatives

Due to the properties of Legendre polynomials, the calculation of derivatives in the current analysis can be obtained by the matrix form [42]:

$$\frac{d\Psi(x)}{dx} = D\Psi(x), \quad (9)$$

where D is a $2^k M \times 2^k M$ derivative matrix defined as follows:

$$D = \begin{pmatrix} F & 0 & \cdots & 0 \\ 0 & F & & 0 \\ \vdots & & \ddots & \vdots \\ 0 & 0 & \cdots & F \end{pmatrix}, \quad (10)$$

where F is a $M \times M$ matrix which is defined as follow:

$$F_{r,s} = \begin{cases} 2^{k+1}\sqrt{(2r-1)(2s-1)}, & r = 2, \dots, M, S = 1, \dots, r-1, \text{and } (r+s) \text{ odd}, \\ 0, & \text{otherwise}. \end{cases} \quad (11)$$

The calculation of derivatives in the spectral space can be easily implemented by multiplying spectral space coefficient C by the derivative matrix D.

3.2 Numerical algorithm

In order to simulate the wave function, a new variable V, the velocity, is introduced as $V = \frac{\partial u}{\partial t}$. Another variable w is introduced by $w = \frac{\partial^2 u}{\partial x^2}$ for simplifying the calculation of boundary conditons. The new governing equations with the fixed boundary condition are as follows:

$$\begin{gathered}
\frac{\partial u}{\partial t} = V, \frac{\partial^2 u}{\partial x^2} = w, \\
\rho \frac{\partial V}{\partial t} = \sigma_x + \nu \frac{\partial^2 V}{\partial x^2} - k_g \frac{\partial^2 w}{\partial x^2} + f, \\
c_v \frac{\partial \theta}{\partial t} = k \frac{\partial^2 \theta}{\partial x^2} + k_1 \theta \varepsilon \frac{\partial \varepsilon}{\partial t}, \\
\sigma = k_1(\theta - \theta_1)\frac{\partial u}{\partial x} - k_2\left(\frac{\partial u}{\partial x}\right)^3 + k_3\left(\frac{\partial u}{\partial x}\right)^5.
\end{gathered} \tag{12}$$

$$\begin{aligned}
&u(0,t) = 0, \quad u(L) = 0, \\
&w(0,t) = 0, \quad w(L,t) = 0, \\
&\theta_x(0,t) = 0, \quad \theta_x(L,t) = 0.
\end{aligned}$$

The corresponding model with the impact boundary conditions is as follows:

$$\begin{gathered}
\frac{\partial u}{\partial t} = V, \frac{\partial^2 u}{\partial x^2} = w, \\
\rho \frac{\partial V}{\partial t} = \sigma_x + \nu \frac{\partial^2 V}{\partial x^2} - k_g \frac{\partial^2 w}{\partial x^2}, \\
c_v \frac{\partial \theta}{\partial t} = k \frac{\partial^2 \theta}{\partial x^2} + k_1 \theta \varepsilon \frac{\partial \varepsilon}{\partial t} \\
\sigma = k_1(\theta - \theta_1)\frac{\partial u}{\partial x} - k_2\left(\frac{\partial u}{\partial x}\right)^3 + k_3\left(\frac{\partial u}{\partial x}\right)^5.
\end{gathered} \tag{13}$$

$$\begin{aligned}
&u(0,t) = 0, \quad \sigma(L,t) = s(t), \\
&w(0,t) = 0, \quad w(L,t) = 0, \\
&\theta_x(0,t) = 0, \quad \theta_x(L,t) = 0.
\end{aligned}$$

By employing the LWM, the given set of differential equations in (12,13) can be converted into Differential Algebraic Equations(DAEs). The mechanical and thermal equations can be recasted into ODEs, and

the stress-strain relationship which is the fourth line of (13) can be discretized into a set of algebraic equations. By combining ODEs and algebraic equations, Eq.(12) and Eq.(13) can be rewritten in the following DAEs form:

$$L\frac{dU}{dt} + N(t, U) = 0, \tag{14}$$

where $U = [u, V, w, \sigma]^T$, L is the linear operator matrix, and N is the nonlinear operator matrix related to t and variants of U. Eq. (14) is a stiff system which is difficult to solve by conventional numerical integration algorithms. To cope with the difficulty, the backward differentiation formula is applied here to discretize the time derivative as follow:

$$L(U^n - U^{n-1}) + \Delta t N(t, U^n) = 0, \tag{15}$$

where n is the current time layer. Iterations are performed by using Newton's method to get U^n from U^{n-1} for each layer, and the stepsize of the time advancing is chosen as $\Delta t = 0.001ms$. The iteration stops when the relative residual is less than $1e^{-4}$.

4 Numerical simulation

The model parameter values for the numerical experiments in the present paper can be found in Ref. [43]. Specifically, we have been using the $Au_{23}Cu_{30}Zn_{47}$ material with the following coefficients:

$k_1 = 480g(ms)^{-4}(cm)^{-2}K^{-2}$, $k_2 = 6 \times 10^6 g(ms)^{-2}(cm)^{-1}K^{-1}$,
$k_3 = 4.5 \times 10^8 g(ms)^{-2}(cm)^{-1}K^{-1}$, $\theta_1 = 208K$, $\rho = 11.1g(cm)^{-3}$,
$k_g = 10g(ms)^{-2}$, $c_v = 29g(ms)^{-2}(cm)^{-1}K^{-1}$,
$k = 1.9 \times 10^{-2} cm\, g(ms)^{-3}K^{-1}$, $\nu = 10g(cm)^{-1}(ms)^{-1}$.

As mentioned in section 3, the LWM is actually an approximation in differential subintervals, therefore, it is important to choose an appropriate boundary condition transfer algorithm. The boundary condition transfer algorithm in the current paper is constructed in a similar way as that for cubic spline functions. For any function, it will be defined as c^2 function across the subinterval boundary, therefore the following relationship at the boundary interface x_i between each subintervals could be formulated:

$$f_{left}(x_i) = f_{right}(x_i),\ \ \frac{\partial f}{\partial x_{left}}(x_i) = \frac{\partial f}{\partial x_{right}}(x_i),\ \ \frac{\partial^2 f}{\partial x^2{}_{left}}(x_i) = \frac{\partial^2 f}{\partial x^2{}_{right}}(x_i). \quad (16)$$

The choices of Legendre wavelets coefficients k and M are also important in the simulations. The coefficient M represents the number of the points in each subinterval, it determines the accuracy and computation time of the simulation. For the same accuracy, increasing k and decreasing M will reduce the computational time. In the current paper, the parameters are chosen as k=6 and M=4. It should be noted that the value of k cannot be too small, since the boundary condition transfer algorithm would require two nodes in each subinterval.

4.1 Dimensionless form of the governing equations

For the numerical experiment, the dimension disunity of the nonlinear terms may cause significant computational difficulties and even affects the convergence of the simulation when the problem is a stiff coupled system. There are many advantages to rescale the equations into a dimensionless form, such as simplifying the calculations and improving numerical stability. Here Eq.(12) and Eq.(13) are rescaled into a dimensionless form by using the following strategy. The least number of co-

efficients would be remained in the new governing equations. Every variable gets a new form here:

$$\varepsilon = \varepsilon_0\tilde{\varepsilon}, x = \delta\tilde{x}, t = t_0\tilde{t}, \theta = \theta_c\tilde{\theta}. \tag{17}$$

Firstly, the coefficients in nonlinear terms of the Landau theory, such as k_1, k_2 and k_3 should be transferred into a dimensionless form: $\varepsilon_0 = \sqrt{\frac{k_2}{k_3}}$. Then, the momentum and energy balance should take the dimensionless form if $\delta = \frac{\sqrt{k_g k_3}}{k_2}$, $t_0 = \frac{\sqrt{\rho k_g} k_3}{k_2^2}$, $\theta_c = 100$. Finally, the mechanical field Eq.(12) and Eq.(13) can be rescaled as follows:

$$\begin{aligned} \frac{\partial\tilde{u}}{\partial\tilde{t}} &= \tilde{V}, \frac{\partial^2\tilde{u}}{\partial\tilde{x}^2} = \tilde{w}, \\ \frac{\partial\tilde{V}}{\partial\tilde{t}} &= \widetilde{\sigma_{\tilde{x}}} + \tilde{v}\frac{\partial^2\tilde{V}}{\partial\tilde{x}^2} - \widetilde{k_g}\frac{\partial^2\tilde{w}}{\partial\tilde{x}^2} + \tilde{f}, \\ \tilde{\sigma} &= \widetilde{k_1}(\theta - \theta_1)\tilde{\varepsilon} - \tilde{\varepsilon}^3 + \tilde{\varepsilon}^5. \end{aligned} \tag{18}$$

The thermal equation can then be written in the following form:

$$\frac{\partial\tilde{\theta}}{\partial\tilde{t}} = \tilde{k}\frac{\partial^2\tilde{\theta}}{\partial\tilde{x}^2} + \widetilde{k_1'}\tilde{\theta}\tilde{\varepsilon}\frac{\partial\tilde{\varepsilon}}{\partial\tilde{t}}, \tag{19}$$

where the new dimensionless coefficients are $\tilde{k} = 6.9 \times 10^{-6}$, $\widetilde{k_1} = 0.6$, $\widetilde{k_1'} = 0.2207$, $\widetilde{k_g} = 1 \times 10^{-4}$, $\tilde{v} = 9.49 \times 10^{-3}$.

4.2 Simulation results

In this section, the numerical results obtained with the above model are discussed. The simulations with both fixed and impact boundary conditions have been carried out.

The first part of numerical simulations is with the impact boundary condition. The stress on the rod right end is regarded as the impact loading since it is a 1-D model. A rectangular loading profile, which is

approximately treated as a pulse stress impact loading, is employed in these simulations:

$$s(t) = \begin{cases} 4000, & 0 \le t \le 0.005\text{ms}, \\ 0, & t > 0.005\text{ms}. \end{cases} \quad (20)$$

This can be convert into the dimensionless form:

$$s(\tilde{t}) = \begin{cases} 0.484, & 0 \le \tilde{t} \le 0.379, \\ 0, & \tilde{t} > 0.379. \end{cases} \quad (20)$$

There should be 6 martensite phases existed during the martensite phase transformations of $Au_{23}Cu_{30}Zn_{47}$, since it is a cubic-to-orthorhombic one. However, according to the Ginzburg-Landau theory, the martensite phase transformations happened in a SMA rod, which means it can be simplified to a 1D situation, only involve one austenite and martensite twins for simplification [21,22,43]. For the numerical analysis, the Landau free energy density function $F = \frac{k_1}{2}(\theta - \theta_1)\varepsilon^2 - \frac{k_2}{4}\varepsilon^4 + \frac{k_3}{6}\varepsilon^6$ is employed. There are three local minima of this function, which represent three phase states: the local minimum $\varepsilon = 0$ represents the austenite phase (A), and the other two symmetric local minima represent two martensitic phases (M^+ and M^-).

The first simulation for the thermo-mechanical model is performed at a low temperature of 210°K. At this temperature, the stress-strain relationship is nonlinear and we have to deal with a hysteresis loop when the stress varies, due to the curve $\widehat{AC}$ is unstable and strain will jump from A to B or C to D [25,37], as sketched in Fig.1. At this temperature, only martensite is stable, so we set the initial condition at M^- state, which means that $\widetilde{u_0} = -0.89\tilde{x}$ and $\widetilde{\varepsilon_0} = -0.89$ [43]. The simu-

lation results are presented in Fig. 2 and Fig.3. The displacement and strain distributions are plotted in Fig.2 (a) and (b), respectively whilst the SMA temperature distribution is plotted in Fig.3. It is shown clearly by Fig.2 (b) that the interface between M^+ and M^- is pushed from the right side to the left side by the impact loading. Under this loading, all the martensite is turned gradually from M^- to M^+. The temperature distribution variation is also like a wave, as sketched in Fig.3. The temperature of SMA material at the interface is much lower than in the other area. This could be easily explained by the fact that there is latent heat needed for the phase transformation induced at the interface. It is also clearly illustrated by Fig.3 that the temperature of the right part of the interface, which has already experienced the martensite phase transformation, is a little higher than on the left side. This phenomenon is consistent with those simulation results reported in literatures [25,26,36]. Thus, the thermo-mechanical coupling effect is captured well in this simulation.

The second numerical simulation with the same boundary conditions is performed with a high temperature at 330°K, and the results are presented in Figs.4, 5 and 6. It is clearly shown by Fig.4 that only one local minimum $\varepsilon = 0$ exists in the Landau free energy density function F, which means that only austenite phase is stable at this temperature. At this temperature, the stress-strain curve is a monotone one. It is also clearly illustrated by the numerical results that the hysteresis loop no longer exists, due to the curve $\widehat{AC}$ is stable and no jump happened here, as sketched in Fig.4. The strain distribution in the SMA rod is very smooth, which could be regarded as a signal that there would be no

phase transformation during the simulation. Thus, when the initial conditions are set to $\widetilde{u_0} = 0, \widetilde{V_0} = 0$, a thermal wave will be induced by the impact loading, as sketched in Fig.6 The thermal wave propagates from the right end to the left end, and bounced back from the end with a pattern very similar to that of the mechanical waves. This thermal wave is induced by a pure mechanical loading and can be easily explained by the thermo-mechanical coupling and the latent heat effects in the SMA materials [37].

The second part of our numerical simulations is carried out with the fixed boundary conditions. The mechanical loading changes as a function of time and is defined as

$$\bar{f} = 0.0484\sin^3(\pi t/2). \tag{21}$$

Under this mechanical loading, the SMA rod should switch between martensitic phase and austenite phase. For this simulation, the temperature is set to $240^{\circ}K$. According to the assumptions, the initial phase state in this simulations should be the austenitic phase, so the initial value of displacements in this section was set to $\widetilde{u_0} = 0$.

The mechanical and temperature initial conditions ($240^{\circ}K$) taken for this simulation allows both martensitic and austenitic phases co-exist. At this temperature, the Landau free energy function has two symmetric local minima, as sketched in Fig.7, which corresponds to the twin martensitic phase, and one central minimum that corresponds to the austenitic phase. The martensite, which only exists when the SMA is under an external thermal or mechanical loading, is metastable at this temperature and it will be transformed into the austenite when the load-

ing is removed. The pseudoelastic effect could be triggered by this process.

The simulation results are presented in Fig.8. It is shown that the austenite phase is transformed into the twin martensitic phase when the absolute value of loading exceeds a certain value. The phase transformations here are induced by the applied mechanical loading. The temperature evolution is also presented in Fig.9. The temperature evolution figure shows a strong nonlinear thermo-mechanical coupling behavior. A sharp change in temperature changes always accompanied by a sharp change of displacement and strain distributions. The thermo-mechanical coupled effects are captured well in this numerical experiment. When the external loading returns to zero, the displacement also returns back to the initial value, which indicates that the SMA rod becomes in the austenitic phase again. This numerical simulation gives a clear demonstration of the pseudoelastic effect, as stated previously.

5 Computational analysis and performance

In this section we provide detail on the two key aspects of computational performance of our developed numerical methodology: (a) efficiency and (b) stability.

5.1 Computation efficiency

In this section, numerical experiments are presented for the isothermal static situation. Specifically, for this case, the terms involving time derivatives are set to zero, therefore Eq. (3) can be written in the ordinary differential equation(ODE) form:

$$k_1(\theta-\theta_1)\frac{\partial^2 u}{\partial x^2}+k_2\left(\frac{\partial u}{\partial x}\right)^2\frac{\partial^2 u}{\partial x^2}+k_3\left(\frac{\partial u}{\partial x}\right)^4\frac{\partial^2 u}{\partial x^2}-k_g\frac{\partial^4 u}{\partial x^4}+f=0, \quad (23)$$

with the same fixed boundary conditions as in (3). The dimensionless form of the governing equations can be obtained from Eq.(18) as :

$$\begin{aligned}\sigma_{\tilde{x}} &= \frac{\partial^4 \tilde{u}}{\partial \tilde{x}^4}-\tilde{f},\\ \sigma &= \widetilde{k_1}\tilde{\varepsilon}+\tilde{\varepsilon}^3+\tilde{\varepsilon}^5,\end{aligned} \quad (24)$$

where $\widetilde{k_1}$ =0.192, $\tilde{f}=0.4$, $\tilde{\varepsilon}=\frac{\partial \tilde{u}}{\partial \tilde{x}}$, the temperature is set to $240^{\circ}K$. Thus, the initial condition is identified with the austenitic phase:

$$\widetilde{u_0(x)}=0\,. \quad (25)$$

As mentioned in Ref. [40], the LWM is expected to be able to effectively reduce the computation cost. For the purpose of illustrating this, a table on computation times with different computation parameters for the same problem is presented. The results on computational efficiency are in line with expectations. Table 1 shows the time for each grid to obtain the specified tolerance error with the norm $\left\|L\frac{dU}{dt}+N(t,x,U)\right\|_2$. It is evident from this table that the time spent increases significantly with the increase of the M value, however it is not sensitive to the change of k. Hence, the calculation time can be reduced by controlling the number of points in one interval and increasing the number of intervals appropriately. However, the coefficient M cannot be too small because of the restriction caused by the matching of adjacent subintervals.

By performing more numerical simulations, it is found that by using different grid points in different subintervals it is also possible to improve further the computation efficiency. An experiment is performed

on a mixed grid with $k = 3, M = 6$ and $k = 4, M = 6$, and the results are presented in Fig.10. The computational time is 123.69s, whilst the error tolerance is almost the same as the one with grid $k = 4, M = 6$, but it takes even less computation time to achieve the convergence.

From these numerical experiments, it is clearly that the wavelets method could be very effective in simulations of the nonlinear thermo-mechanical dynamics with phase transformation, when the computation parameters are appropriately set. Meanwhile, the method could be improved even further by constructing adaptive grids based on the wavelets methods.

5.2 Stability

In order to avoid the appearance of Runge's phenomenon, the conventional spectral methods such as the Chebyshev method divide the difference interval non-uniformly in such a way that the grid points are dense at the boundary and sparse in the central area. However, martensite phase transition boundaries always occur in the central area. This can be avoided by increasing k value in the LWM. Therefore, the spectral wavelet methods have natural advantages over the conventional ones.

In order to demonstrate these advantages, including stability properties, of the Legendre wavelets method, the same dynamic numerical experiment with fixed boundary conditions is carried out by one of the conventional spectral methods, namely the Chebyshev method. The Matlab function Chebfun [44], based on the Chebyshev method, is used here for comparison. The same optimization and time discretization

strategies are applied here. However, the results are not as good as the results of the LWM. With the same coefficients in section4.1, the Chebfun results are unstable and the term of the domain wall energy fails to control the function, which can be seen in Fig.11. To let it works again, the dimensionless form must be modified to increase the new value of $\widetilde{k_g}$ when it is less than 1. For the new results ($\widetilde{k_g} = 1$), both methods would work. However, it is clearly seen in Fig.12 that the simulation results obtained with Chebfun are still worse than those obtained with the LWM, in particular in its ability to describe the boundary interface of martensite phase transformation. It does not successfully simulate the boundary interface. Chebfun is a good method, but the conclusion can be drawn that the LWM is more robust than Chebfun in the context of our problems.

6 Conclusions

In the current paper, a fully coupled thermo-mechanical model has been adopted to simulate the microstructure evolution of a SMA rod under impact loadings and periodic mechanical loadings. The phase transformation process with both fixed and impact boundary conditions has been successfully simulated via the Legendre wavelets method. The numerical algorithm for solving the coupled nonlinear system of partial differential equations has been presented in detail. The microstructure evolutions induced by impact loadings have been analyzed in detail with different initial conditions. The advantages of the Legendre wavelets method for the SMA modeling have been highlighted and computational performance has been analyzed.

Acknowledgements

This work has been supported by the National Natural Science Foundation of China (Grant No.51575478 and Grant No.61571007), the National Sciences and Engineering Research Council (NSERC) of Canada, and the Canada Research Chair Program. RM is also acknowledging support of the BERC 2018-2021 program and Spanish Ministry of Science, Innovation and Universities through the Agencia Estatal de Investigacion (AEI) BCAM Severo Ochoa excellence accreditation SEV-2017-0718.

Reference

1. Birman V. Review of Mechanics of Shape Memory Alloy Structures[J]. Applied Mechanics Reviews, 1997, 50(11), 629-645.
2. Leo D J, Buckley S J. Vehicular Applications of Smart Material Systems[J]. Proc Spie, 1998, 106–16.
3. Hartl D J, Lagoudas D C. Aerospace applications of shape memory alloys[J], Proc Inst Mech Eng, Part G: J Aerospace Eng., 221 (2007), 535-552.
4. Birman V, Chandrashekhara K, Sain S. An approach to optimization of shape memory alloy hybrid composite plates subjected to low-velocity impact[J]. Composites Part B Engineering, 1996, 27(5), 439-446.
5. Yang C S W, Desroches R, Leon R T. Design and analysis of braced frames with shape memory alloy and energy-absorbing hybrid devices[J]. Engineering Structures, 2010, 32(2), 498-507.
6. Boyd J G, Lagoudas D C. Thermomechanical Response of Shape Memory Composites[J]. Journal of Intelligent Material Systems and Structures, 1994, 5(3), 333-346.
7. Entchev P B, Lagoudas D C. Modeling porous shape memory alloys using micromechanical averaging techniques[J]. Mechanics of Materials, 2002, 34(1), 1-24.
8. Guthikonda V S R, Kiran M K, Sivakumar S M, et al. On smeared and micromechanical approaches to modeling martensitic transformations in SMA[J]. Nonlinear Analysis Real World Applications, 2008, 9(3), 990-1011.
9. Sepe V, Auricchio F, Marfia S, et al. Micromechanical analysis of porous SMA[J]. Smart Materials and Structures, 2015, 24(8), 085035.
10. Lagoudas D C, Ravi-Chandar K, Sarh K, et al. Dynamic loading of polycrystalline shape memory alloy rods[J]. Mechanics of Materials, 2003, 35(7), 689-716.
11. Bo Z, Lagoudas D C. A unified thermodynamic constitutive model and finite element analysis of active metal matrix composites[J]. Proceedings of SPIE - The International Society for Optical Engineering, 1995, 3(2), 153-179.
12. Lagoudas D, Hartl D, Chemisky Y, et al. Constitutive model for the numerical analysis of phase transformation in polycrystalline shape memory alloys[J]. International Journal of Plasticity, 2012, s 32–33(2):155-183.

13. Patoor E, Lagoudas D C, Entchev P B, et al. Shape memory alloys, Part I: General properties and modeling of single crystals[J]. Mechanics of Materials, 2006, 38(5–6), 391-429.
14. Lagoudas D C, Entchev P B, Popov P, et al. Shape memory alloys, Part II: Modeling of polycrystals[J]. Mechanics of Materials, 2006, 38(5–6), 430-462.
15. Hartl D J, Chatzigeorgiou G, Lagoudas D C. Three-dimensional modeling and numerical analysis of rate-dependent irrecoverable deformation in shape memory alloys[J]. International Journal of Plasticity, 2010, 26(10), 1485-1507.
16. Tsouknidas A, Michailidis N, Maliaris G, et al. A numerical study of "functional fatigue" of closed-cell NiTi shape memory foams[J]. Mechanics of Materials, 2019, 131, 11-21.
17. Lester B T, Baxevanis T, Chemisky Y, et al. Review and perspectives: shape memory alloy composite systems[J]. Acta Mechanica, 2015, 226(12), 3907-3960.
18. Tanaka K, A thermomechanical sketch of shape memory effect: one-dimensional tensile behavior[J]. Res.Mechanica, 1986, 18, 251-263.
19. Takahashi Y, Kondo H, Asano R, et al. Direct evaluation of grain boundary hydrogen embrittlement: a micro-mechanical approach[J]. Materials Science and Engineering: A, 2016, 661, 211-216.
20. Takahashi Y, Aihara K, Ashida I, et al. Evaluation of interfacial fracture strength in micro-components with different free-edge shape[J]. Mechanical Engineering Journal, 2016, 3(6): 16-00108-16-00108.
21. Falk F, Model free energy, mechanics, and thermodynamics of shape memory alloys[J]. Acta Metallurgica, 1980, 28(12), 1773-1780.
22. Falk F, Landau theory and martensitic phase transitions[J]. Journal de Physique, 1982, 43(C4), 3-15.
23. Falk F, One-dimensional model of shape memory alloys[J]. Archives of Mechanics, 1983, 35, 63-84.
24. Sprekels J. Global existence for thermomechanical processes with nonconvex free energies of Ginzburg-Landau form[J]. Journal of Mathematical Analysis and Applications, 1989,141(2), 333–348.
25. Bubner N. Landau-Ginzburg model for a deformation-driven experiment on shape memory alloys[J]. Continuum Mechanics & Thermodynamics, 1996, 8(5), 293-308.
26. Berti V, Fabrizio M, Grandi D. Phase transitions in shape memory alloys: A non-isothermal Ginzburg–Landau model[J]. Physica D, 2010, 239(1-2):95-102.
27. Dhote R P, Gomez H, Melnik R V N, et al. Shape memory alloy nanostructures with coupled dynamic thermo-mechanical effects[J]. Computer Physics Communications, 2015, 192, 48-53.
28. Dhote R P, Fabrizio M, Melnik R V N, et al. A three-dimensional non-isothermal Ginzburg–Landau phase-field model for shape memory alloys[J]. Modelling and Simulation in Materials Science and Engineering, 2014, 22(8), 085011.
29. Dhote R P, Melnik R V N, Zu J. Dynamic multi-axial behavior of shape memory alloy nanowires with coupled thermo-mechanical phase-field models[J]. Meccanica, 2014, 49(7), 1561-1575.
30. Dhote R P, Gomez H, Melnik R V N, et al. Isogeometric analysis of a dynamic thermo-mechanical phase-field model applied to shape memory alloys[J]. Computational Mechanics, 2014, 53(6), 1235-1250.
31. Dhote R P, Fabrizio M, Melnik R V N, et al. Hysteresis phenomena in shape memory alloys by non-isothermal Ginzburg–Landau models[J]. Communications in Nonlinear Science and Numerical Simulation, 2013, 18(9), 2549-2561.
32. Dhote R P, Melnik R V N, Zu J. Dynamic thermo-mechanical coupling and size effects in finite shape memory alloy nanostructures[J]. Computational Materials Science, 2012, 63, 105-117.

33. Melnik R V N, Roberts A J, Thomas K A. Computing dynamics of copper-based SMA via centre manifold reduction of 3D models[J]. Computational Materials Science, 2000, 18(3-4):0-268.
34. Dhote R P, Gomez H , Melnik R V N, et al. Effect of Aspect Ratio and Boundary Conditions in Modeling Shape Memory Alloy Nanostructures with 3D Coupled Dynamic Phase-Field Theories[J]. Mathematical Problems in Engineering, 2016, 2016, 1-19.
35. Dhote R P, Gomez, H, Melnik R V N, & Zu, J. 3D coupled thermo-mechanical phase-field modeling of shape memory alloy dynamics via isogeometric analysis[J]. Computers & Structures, 2015, 154, 48–58.
36. Wang L X, Melnik R V N, Simulation of phase combinations in shape memory alloys patches by hybrid optimization methods[J]. Applied Numerical Mathematics, 2008, 58(4), 511-524.
37. Wang L X, Melnik R V N, Thermo-mechanical wave propagation in shape memory alloy rod with phase transformations[J]. Mechanics of Advanced Materials and Structures, 2007, 14 (8), 665-676.
38. Wang L X, Melnik R V N, Numerical model for vibration damping resulting from the first order phase transformations, Applied Mathematical Modelling, 2007, 31, 2008-2018.
39. Wang L X, Melnik R V N. Nonlinear dynamics of shape memory alloy oscillators in tuning structural vibration frequencies[J]. Mechatronics, 2012, 22(8), 1085-1096
40. Razzaghi M, Yousefi S, Legendre wavelets method for the solution of nonlinear problems in the calculus of variations, Mathematical and Computer Modelling, 2001, 34.1–2, 45-54,
41. Bubner N, Mackin G, Rogers R C. Rate dependence of hysteresis in one-dimensional phase transitions[J]. Computational Materials Science, 2000, 18(3-4), 0-254.
42. Mohammadi F, Hosseini M M, A new Legendre wavelet operational matrix of derivative and its applications in solving the singular ordinary differential equations[J]. Journal of the Franklin Institute, 2011, 348.8, 1787-1796.
43. Melnik R V N, Roberts A J, Thomas K A. Phase transitions in shape memory alloys with hyperbolic heat conduction and differential-algebraic models[J]. Computational Mechanics, 2002, 29(1), 16-26.
44. Driscoll T A, Hale N, and Trefethen L N, editors, Chebfun Guide, Pafnuty Publications, Oxford, 2014.

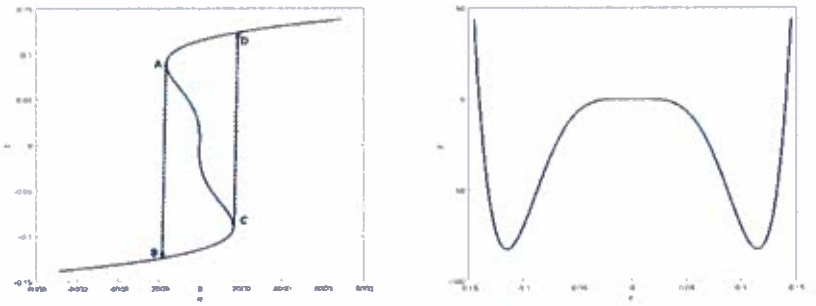

Fig. 1 (a) Relationship of stress and strain and (b) figure of the Landau free energy density function at 210°K

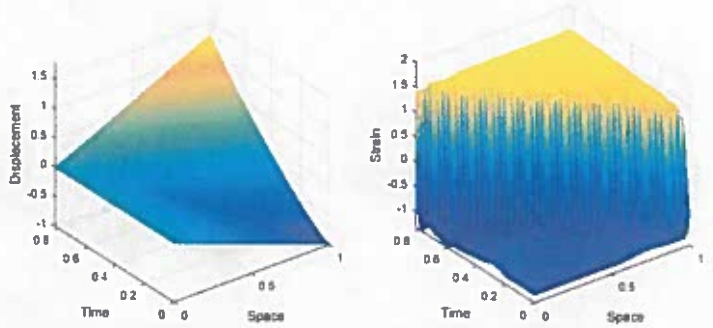

Fig.2 (a) Displacement and (b)strain microstructures evolution at *210°K*

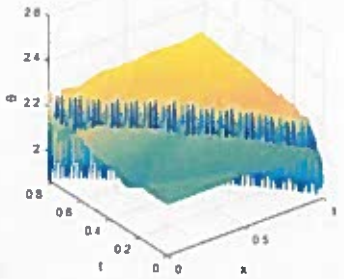

Fig. 3 Temperature evolution with initial value at *210°K*.

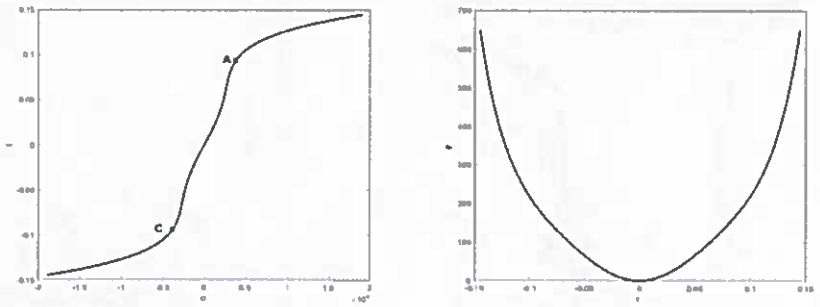

Fig. 4 (a)Relationship of stress and strain and (b)figure of the Landau free energy density function at *330°K*

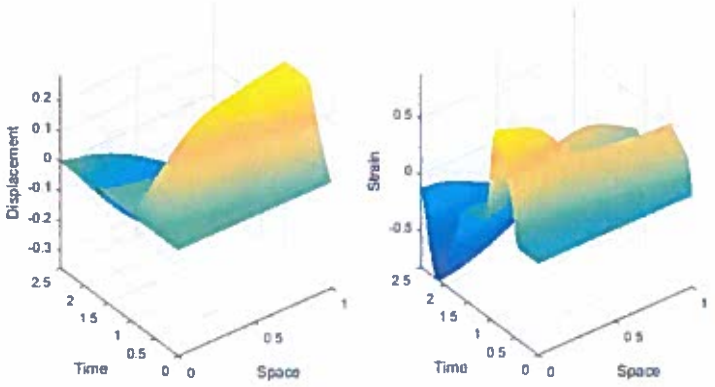

Fig. 5 (a)Displacement and (b)strain microstructures evolution at *330°K*

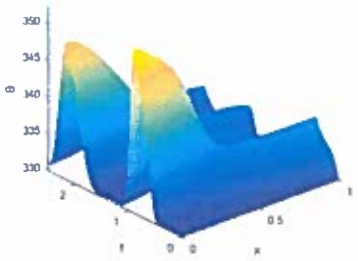

Fig. 6 Temperature evolution at *330°K*

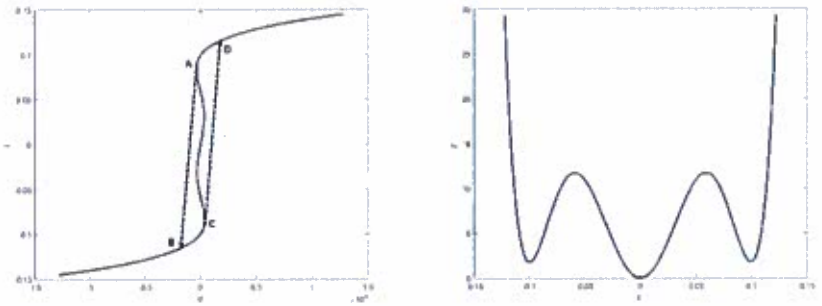

Fig. 7 (a) Relationship of stress and strain and(b) figure of Landau free energy function at 240°K

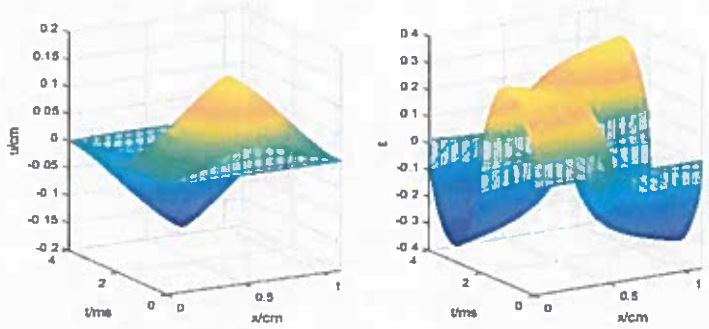

Fig.8 The simulation results of microstructure at 240°K: (a) displacement; (b) strain

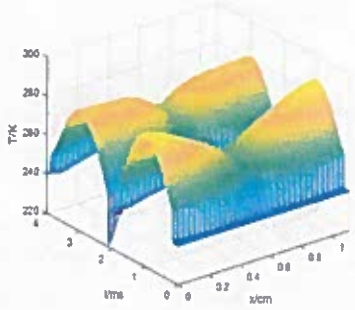

Fig. 9 The temperature evolution at 240°K

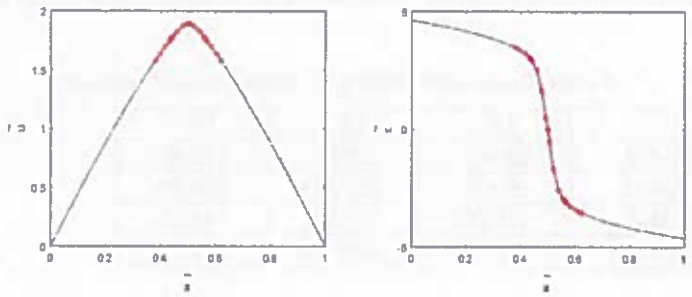

Fig. 10 (blue line) k=3, M=6; (red line) k=4, M=6

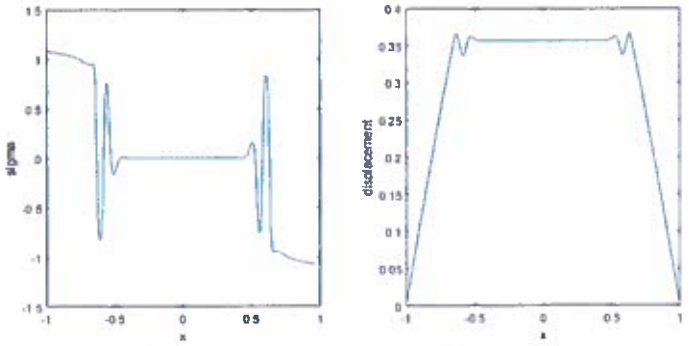

Fig. 11 The unstable results at $\tilde{t}$=0.95 when $\widetilde{k_g} = 1 \times 10^{-4}$

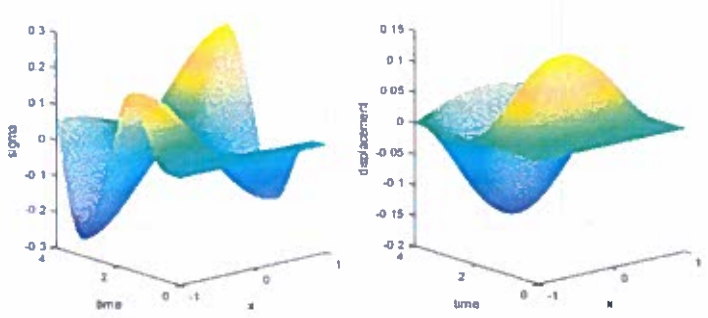

Fig. 12 The simulation results of microstructure via Chebfun: (a) strain; (b) displacement.

Table 1. The calculation times with different grids and accuracies.

	10^{-2}	10^{-3}	10^{-4}
k=2,M=6	93.40s	108.05s	115.45s
k=3,M=6	99.57s	116.52s	120.65s
k=4,M=6	115.00s	123.98s	148.51s
k=2,M=12	402.74s	429.18s	452.29